SCIENCE CHINA Materials ARTICLES

mater.scichina.com link.springer.com

Published online 18 January 2021 | https://doi.org/10.1007/s40843-020-1548-x
Sci China Mater 2021, 64(6): 1507–1520

Achieving superior performance in thermoelectric $Bi_{0.4}Sb_{1.6}Te_{3.72}$ by enhancing texture and inducing high-density line defects

Junhao Qiu[1], Yonggao Yan[1*], Hongyao Xie[2], Tingting Luo[1], Fanjie Xia[1], Lei Yao[1], Min Zhang[1], Ting Zhu[1], Gangjian Tan[1], Xianli Su[1], Jinsong Wu[3], Ctirad Uher[4], Hongyi Jiang[1] and Xinfeng Tang[1*]

ABSTRACT **Miniaturization of efficient thermoelectric (TE) devices has long been hindered by the weak mechanical strength and insufficient heat-to-electricity conversion efficiency of zone-melted (ZM) ingots. Here, we successfully prepared a robust high-performance p-type $Bi_{0.4}Sb_{1.6}Te_{3.72}$ bulk alloy by combining an ultrafast thermal explosion reaction with the spark plasma sintering (TER-SPS) process. It is observed that the introduced excess Te not only enhances the (00*l*)-oriented texture to ensure an outstanding power factor (PF) of 5 mW m^{-1} K^{-2}, but also induces extremely high-density line defects of up to 10^{11}–10^{12} cm^{-2}. Benefiting from such heavily dense line defects, the enhancement of the electronic thermal conductance from the increased electron mobility is fully compensated by the stronger phonon scattering, leading to an evident net reduction in total thermal conductivity. As a result, a superior *ZT* value of ~1.4 at 350 K is achieved, which is 40% higher than that of commercial ZM ingots. Moreover, owing to the strengthening of grain refinement and high-density line defects, the mechanical compressive stress reaches up to 94 MPa, which is 154% more than that of commercial single crystals. This research presents an effective strategy for the collaborative optimization of the texture, TE performance, and mechanical strength of Bi_2Te_3-based materials. As such, the present study contributes significantly to the future commercial development of miniature TE devices.**

Keywords: thermoelectric, Bi_2Te_3, texture, line defect, micro device

INTRODUCTION

Thermoelectric (TE) technologies enable direct conversion between electricity and heat, which are irreplaceable in certain applications, such as independent power sources and precise temperature control [1–4]. The widespread application of laser diode cooling in 5G communication and the emergence of wearable smart electronic devices, have recently initiated a substantial demand for efficient miniature TE modules [5–7]. The energy conversion efficiency of TE modules is contingent on the dimensionless figure-of-merit defined as $ZT = S^2\sigma T/\kappa$, where S, σ, κ and T are the Seebeck coefficient, electrical conductivity, total thermal conductivity, and absolute temperature, respectively [8–13]. Therefore, a large Seebeck coefficient, high electrical conductivity and thermal conductivity as low as possible are essential in a superior TE material [14–16]. However, the three basic parameters are intimately coupled with each other, making it a considerable challenge for synergistically optimizing electronic and thermal transport properties to achieve an exceptional TE performance [17–21].

Bi_2Te_3-based materials are well-known for having multiple degenerate bands, a narrow band gap and large molecular weight, which have been the preferred TE compounds at near room temperature for decades [22,23]. Along the crystallographic *c*-axis, Bi_2Te_3 crystals (space group $R\bar{3}m$) are comprised of quintuple layer units with the -$Te^{(1)}$-Bi-$Te^{(2)}$-Bi-$Te^{(1)}$- stacking [24]. Adjacent quintuple layers are bonded by weak van der Waals forces, whereas the inner layers are primarily composed of covalent and ionic bonds [25,26]. Moreover, Bi_2Te_3 crystals exhibit a significant degree of anisotropy, namely, the electronic transport property along the (00*l*) atomic

[1] State Key Laboratory of Advanced Technology for Materials Synthesis and Processing, Wuhan University of Technology, Wuhan 430070, China
[2] Department of Chemistry, University of Northwestern, Evanston, Illinois 60208, United States
[3] Nanostructure Research Center, Wuhan University of Technology, Wuhan 430070, China
[4] Department of Physics, University of Michigan, Ann Arbor, Michigan 48109, United States
* Corresponding authors (emails: yanyonggao@whut.edu.cn (Yan Y); tangxf@whut.edu.cn (Tang X))

plane is markedly superior to other atomic planes. The peak *ZT* value of highly textured Bi_2Te_3-based single crystals conventionally grown by zone melting (ZM) is still around unity. Furthermore, the ZM process is rather time- and energy-intensive [27–30]. More importantly, the easy cleavage of single crystals along the basal plane results in poor mechanical strength. Therefore, it is almost impossible to use ZM ingots for the fabrication of miniature TE devices. Numerous researchers have thereby attempted to obtain nano-sized polycrystalline by mechanical alloying (MA) [14] and melt spinning (MS) [31–34]. A significant decrease in the lattice thermal conductivity and substantial enhancement of the mechanical strength can be achieved simultaneously due to the grain refinement. The key characteristic of the texture, however, is inevitably sacrificed for the completely disordered grain alignment. The carrier mobility is thus suppressed, producing only modest electrical conductivity and further lowering the power factor (PF).

Texture engineering, fortunately, offers a promising approach to overcome the aforementioned challenge to some extent [35–38]. It is evident that achieving a high texture degree in Bi_2Te_3-based materials requires grains to be aligned in one direction as much as possible. The introduction of temperature gradient [39,40], magnetic field [41] and axial pressure [23,42,43] during the recrystallization process has been typically used to induce the directional alignment of grains along a specific direction. Meanwhile, the (00*l*) atomic plane possesses the lowest stacking fault energy, resulting in the generation of line defects characterized by an additional half-plane of atom during non-equilibrium solidification or plastic deformation [44–47]. Such line defects are assumed to be able to effectively scatter numerous mid-frequency phonons, markedly reducing the lattice thermal conductivity, whilst exerting only a marginal influence on the carrier mobility. Therefore, by enhancing the texture by incorporating dynamic recrystallization, it is possible to increase the carrier mobility and optimize the electrical properties. Meanwhile, the induced high-density defects (point and line defects, etc.) can block the phonon transport very effectively. The increase in the electronic thermal conductivity due to the enhanced mobility is potentially compensated by an even greater decrease in the lattice thermal conductivity, leading to a net reduction in the total thermal conductivity [48]. Therefore, the unique crystal structure of Bi_2Te_3-based alloys offers an opportunity for synchronous optimization of the electrical and thermal transport properties through rational texturing engineering.

Hot deformation (HD) methods, involving hot forging and extrusion, have been used to synergistically optimize the texture and TE performance [29,49–51]. In 2019, Wu *et al.* [51] adopted a liquid phase HD method to enhance the TE performance of n-type Bi_2Te_3-based solid solutions and found a liquid eutectic phase, facilitating the rotation of grains and therefore leading to an enhanced (00*l*)-oriented texture and carrier mobility. Nevertheless, such a liquid-phase HD method involves complex processes and is thus, time- and energy-consuming. More importantly, the donor-like effect during the pulverization process would potentially stimulate the large fluctuation in the carrier concentration and poor repeatability of TE properties. Hence, it is imperative to develop a simple technology to prepare Bi_2Te_3-based polycrystalline materials with a certain degree of texture, superior electrical and thermal transport properties, whilst preserving an excellent mechanical strength.

In the present study, we synthesized a series of $Bi_{0.4}Sb_{1.6}Te_{3+x}$ compounds using a rapid thermal explosion reaction with spark plasma sintering (TER-SPS) technique. To produce a flowing liquid phase during sintering, different amounts of excess Te were added in the TER process. The effects of excess Te on the phase composition, microstructure, TE and mechanical performance of sintered bulk samples were systematically investigated. Due to the enhanced texture and the properly sized grains, an exceptional electronic transport property was obtained in the Te-rich $Bi_{0.4}Sb_{1.6}Te_{3.72}$ sample, with its maximum PF up to 5 mW m^{-1} K^{-2} at room temperature, 31% higher than the value measured in the stoichiometric $Bi_{0.4}Sb_{1.6}Te_3$ sample. Moreover, the multiple-shaped and highly dense line defects were randomly distributed on the plane perpendicular to the sintering pressure, reducing the lattice thermal conductivity dramatically. Finally, the peak *ZT* value of 1.4 at 350 K was achieved in the $Bi_{0.4}Sb_{1.6}Te_{3.72}$ sample, 22% larger than that of the $Bi_{0.4}Sb_{1.6}Te_3$ sample. Simultaneously, the $Bi_{0.4}Sb_{1.6}Te_{3.72}$ sample also demonstrated excellent mechanical strength. This research provides a simple and effective method to simultaneously optimize the texture, TE and mechanical properties of Bi_2Te_3-based compounds. It provides a solid foundation for the commercialization of Bi_2Te_3-based polycrystalline materials and the fabrication of miniature TE modules.

EXPERIMENTAL SECTION

Sample preparation

In reference to the stoichiometric ratio of $Bi_{0.4}Sb_{1.6}Te_{3+x}$ (x = 0, 0.18, 0.36, 0.54, 0.72), Bi (99.999%, 200 mesh), Sb

(99.999%, 200 mesh) and Te (99.999%, 200 mesh) powder materials were weighed and blended in an agate mortar for more than 30 min in air and then cold-pressed into a columnar pellet by a steel die under 20 MPa for 5 min. The pellet was then sealed in a quartz tube under vacuum and placed into a muffle furnace maintained at 883 K for approximately 5 min to initiate the thermal explosion reaction and obtain the objective products. After the products were pulverized into powder, bulk samples were prepared by SPS (Ed-PAS-III, Elenix, Japan) in vacuum under 40 MPa at 723 K with a heating rate of 100 K min^{-1}.

Sample characterization

Powder X-ray diffraction XRD (XRD) (PANalytical, Empyrean, Netherlands) was used to identify the phases of the prepared samples. By combining a field emission scanning electron microscope (Hitachi FESEM, SU8020, Japan) with a high-resolution transmission electron microscope (HRTEM) (Talos F200S, Thermo Fisher, USA), morphologies could be investigated. The back-scattered electron images and the actual composition were obtained by an electron-probe microanalysis (EPMA) (JXA-8230, JEOL, Japan). The basic electrical transport properties, such as electrical conductivity and Seebeck coefficient, were obtained simultaneously by using a commercial ZEM-3 (UlvacRiko, Inc.) instrument. The room-temperature Seebeck coefficient and its distribution were tested by a potential-Seebeck-microprobe instrument (Panco PSM, Germany). The Hall coefficient R_H and electrical conductivity at low temperature from 10 to 300 K were measured by a physical property measurement system (PPMS-9) (Quantum Design, USA). The hole concentration (p) and mobility (μ) were then obtained by using the equations: $p = 1/(eR_H)$ and $\mu = \sigma R_H$, respectively. The thermal transport property, namely the thermal conductivity (κ) was calculated by the equation $\kappa = DC_pd$, where D is the thermal diffusivity coefficient measured by a laser flash method (LFA-457, Netzch, German), C_p is the specific heat determined by a differential scanning calorimeter (DSC) (Q20, TA Instrument, USA), and d is the density obtained by the Archimedes method. The mechanical compressive property was tested by mechanical testing instrument (MTS) (E44.104, China). The cutting test of the bulk sample was conducted by a precision dicing machine (DS613, Heyan Technology, China).

RESULTS AND DISCUSSION

Phase and microstructure

Fig. S1 presents the powder XRD patterns and DSC curves of the as-reacted $Bi_{0.4}Sb_{1.6}Te_{3+x}$ products after thermal explosion. As depicted in Fig. S1a, the main diffraction peaks of all samples are indexed with the reference pattern of $Bi_{0.4}Sb_{1.6}Te_3$ (JCPDS: 01-072-1836), suggesting that the main phase of the as-reacted products is $Bi_{0.4}Sb_{1.6}Te_3$. Fig. S1c demonstrates that the characteristic peak of Te at 27.5° appears in each sample and the peak obviously intensifies with the increasing excess of Te. It is deduced that different amounts of excess Te still remain in the as-reacted products, even for the stoichiometric $Bi_{0.4}Sb_{1.6}Te_3$ sample. Fig. S2 and Table S1 further indicate that the excess Te randomly distributes as the $Bi_{0.4}Sb_{1.6}Te_3$-Te eutectic phase along with a small amount of free Te. As shown in Fig. S1b, d, the endothermic peak at approximately 693 K is due to the melting of the $Bi_{0.4}Sb_{1.6}Te_3$-Te eutectic phase during the heating process. With the increasing excess of Te, the peak temperature shifts higher and the heat absorption gradually intensifies.

Fig. 1a, b present the XRD patterns of SPS-sintered bulk samples, collected on the planes perpendicular (denoted as ⊥) and parallel (marked by //) to the sintering pressure, respectively. It is discovered that the characteristic peak of Te disappears in all samples, indicating that the sintered bulk materials are pure phases. Essentially, as depicted in Fig. S3, under the sintering temperature of 460°C, the excess Te will be squeezed out during the SPS due to the lower melting points of the eutectic phase (420°C) and the free Te element (450°C). Thus, no residual Te-containing impurities remain in the sintered bulk materials. Furthermore, the intensity of (00l) diffraction peak collected on the ⊥ plane in Fig. 1a is augmented as the amount of excess Te increases. In contrast, the (110) diffraction peak on the // plane intensifies as x increases, whereas the (00l) peaks gradually disappear, as shown in Fig. 1b, which reflects the texture features of the sintered samples. Fig. 1c illustrates the DSC curves recorded during the heating and cooling cycles for the sintered materials. Temperatures of the endothermic and exothermic peaks for all samples are almost the same, at approximately 693 K. It is worth acknowledging that a slight deviation between peak temperatures in the heating and cooling cycles is caused by the temperature overshot and hysteresis during the DSC process. Fig. S4 presents the back-scattered-electron (BSE) images of all bulk materials, indicating that they are single phases with no excess of Te. To quantitatively evaluate the degree of texture of the sintered bulk, the orientation factor F is determined by Equations (1)–(3) [39],

$$F = \frac{P - P_0}{1 - P_0}, \quad (1)$$

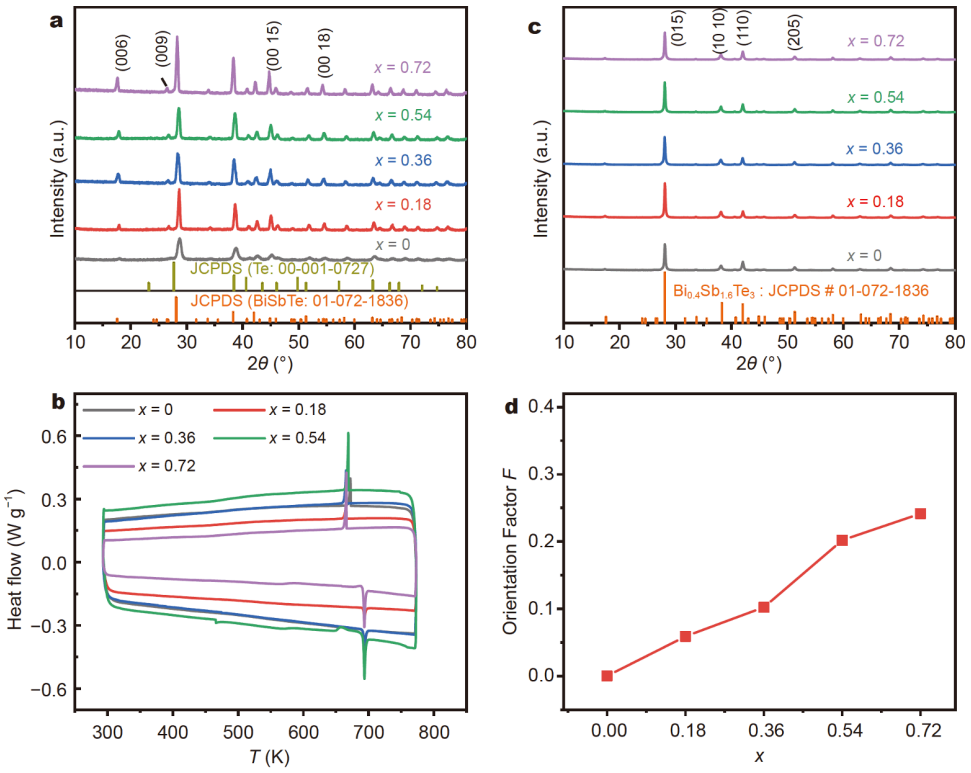

Figure 1 XRD patterns of the SPS-prepared bulk samples, collected on the planes (a) perpendicular (⊥) and (b) parallel (//) to the sintering pressure direction, respectively. (c) Heat flow curves of the sintered bulk samples during heating and cooling. (d) Relationship between the orientation factor F and the amount of introduced excess Te.

$$P_0 = \frac{\sum I_0(00l)}{\sum I_0(hkl)}, \tag{2}$$

$$P = \frac{\sum I(00l)}{\sum I(hkl)}, \tag{3}$$

where $I(hkl)$ and $I(00l)$ are intensities of the (hkl) and $(00l)$ diffraction peaks in bulk samples, respectively, and I_0 (hkl) and $I_0(00l)$ are intensities of the (hkl) and $(00l)$ diffraction peaks of the randomly oriented powder specimens, respectively. The larger the orientation factor F, the stronger the texture. Fig. 1d demonstrates that F gradually increases with the rising amount of Te excess. The orientation factor of the $x = 0.72$ sample can reach up to 0.25, much higher than that of the $x = 0$ sample. Fig. 2a–e show the SEM images of the fracture plane taken from the ⊥ cross-sections of bulk samples. It is clearly observed that the randomly orientated grains gradually transform to the preferential lamellar grains when x increases from 0 to 0.72. This trend is consistent with the results of SEM images taken from the // fracture planes, as shown in Fig. 2f–j, further demonstrating that the texture of the $Bi_{0.4}Sb_{1.6}Te_{3+x}$ bulk sample is enhanced with the rising Te amount.

Defect microstructure

To further elucidate the effect of excess Te on the microstructure of as-prepared bulk materials, it was necessary to conduct a comprehensive TEM observation on the $Bi_{0.4}Sb_{1.6}Te_{3+x}$ (x = 0, 0.72) samples. Fig. S5 provides the spatial orientation relationship between the observed TEM sample and the SPS pressure direction. Initially, the TEM microstructure was analyzed on the ⊥ plane of the $Bi_{0.4}Sb_{1.6}Te_3$ bulk sample, as shown in Fig. S6. As observed, almost no line defects appear on the clean surfaces of grains, no lattice distortion in the corresponding inverse fast Fourier transform (IFFT) images, displayed in Fig. S6b, c. The *in-situ* TEM-energy-dispersive X-ray spectroscopy (EDS) analyses in Fig. S6d, e demonstrate the homogeneous element distribution and the same chemical composition as the nominal stoichiometry. In comparison, the TEM microstructure on the ⊥ plane in the $Bi_{0.4}Sb_{1.6}Te_{3.72}$ sample is also observed, as presented in Fig. 3. There are three different shapes of highly dense

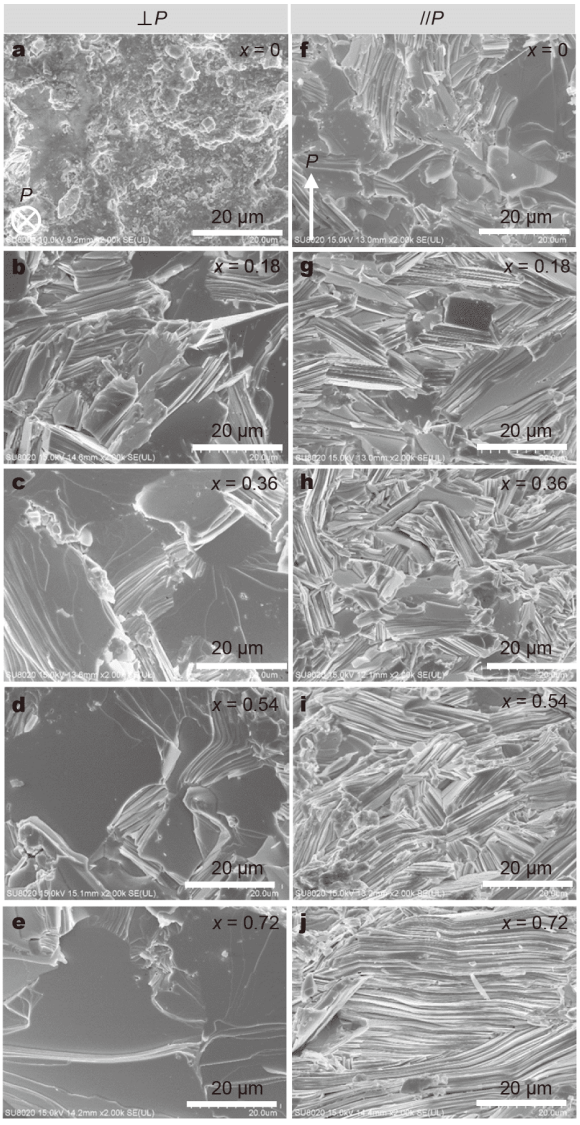

Figure 2 FESEM images of the $Bi_{0.4}Sb_{1.6}Te_{3+x}$ bulk samples, observed on fracture planes (a–e) perpendicular (⊥) and (f–j) parallel (//) to the pressure direction, respectively.

line defects observed inside the grains, namely (i) "S" type, (ii) "X" type and (iii) "Reticular" type, as shown in Fig. 3a–c, respectively. Interestingly, the "S" type line defects are in a zigzag array and well-arranged, whereas "X" type defects cross each other, and the "Reticular" type defects exhibit a random arrangement and interweaving. Mion *et al.* [52] reported that a dislocation density above 10^7 cm^{-2} would exert a significant effect by reducing the lattice thermal conductivity of GaN. In the present study, the number of dislocation lines per unit area was used in Fig. 3a–c to statistically estimate the areal density of line defects (N_D). The statistically average N_D is estimated at 10^{11}–10^{12} cm^{-2}. This is an extremely high value compared with the previously reported 10^9–10^{10} cm^{-2} in several Bi_2Te_3-based materials with arrays of dislocations at grain boundaries [44,45]. Therefore, the ultra-high N_D observed in this research is sufficient evidence to support Klemens' claim regarding mid-frequency phonon scattering reducing the lattice thermal conductivity [53]. Fig. 3d–f illustrate the locally magnified HRTEM images of line defects in the white boxes shown in Fig. 3a–c, respectively. Each of them displays the evident bright and dark color contrasts. The dark region is generally considered the strain contrast arising as a consequence of dislocation and lattice distortions, which is more clearly observed by the atomic-resolved HRTEM image in Fig. 3f, presenting an additional half-plane of atoms and severe lattice distortion. The distorted region has the width of only a few atoms, thus exhibiting a long and narrow line. Fig. 3g–i are the IFFT images of (015), (300) and (104) atomic planes, respectively. They demonstrate the evident light and dark contrast caused by the high-density line defects and severe lattice distortions. Corresponding to Fig. 3c, Fig. S7 presents the TEM-EDS results including the elemental mapping and composition. In the region with high-density reticular line defects, the elements distribute homogeneously and exhibit an almost stoichiometric composition of $Bi_{0.4}Sb_{1.6}Te_3$. This result, associated with the aforementioned TEM observations, demonstrates that these high-density line defects are indeed generated from microstructure fluctuations rather than compositional variations and/or the secondary phases.

The TEM microstructure observed on the // plane in the $Bi_{0.4}Sb_{1.6}Te_{3.72}$ sample is also depicted in Fig. S8. It is found that the grain surfaces are extremely clean and barely contain line defects and lattice distortions. Thus, the N_D (//) is markedly lower than N_D (⊥), suggesting that line defects in the $Bi_{0.4}Sb_{1.6}Te_{3.72}$ sample exhibit a strong anisotropy. It is worth noting that the dense dislocations with Moiré fringes at grain boundaries are not observed, as depicted in Fig. S9, which is markedly different from the results reported by Kim *et al.* [44] and Deng *et al.* [54]. To intuitively comprehend the effect of high-density line defects on the lattice strain field, the atomic-scale strain distributions of $x = 0$ and $x = 0.72$ specimens were characterized by geometric phase analysis (GPA), as shown in Fig. 4. It is apparent that the strain field fluctuation in the $x = 0.72$ sample is more evident than in the $x = 0$ sample. A considerable lattice distortion exists around line defects, inducing the local stress and strain field that is usually regarded as the scattering centers disrupting the propagation of mid-frequency phonons.

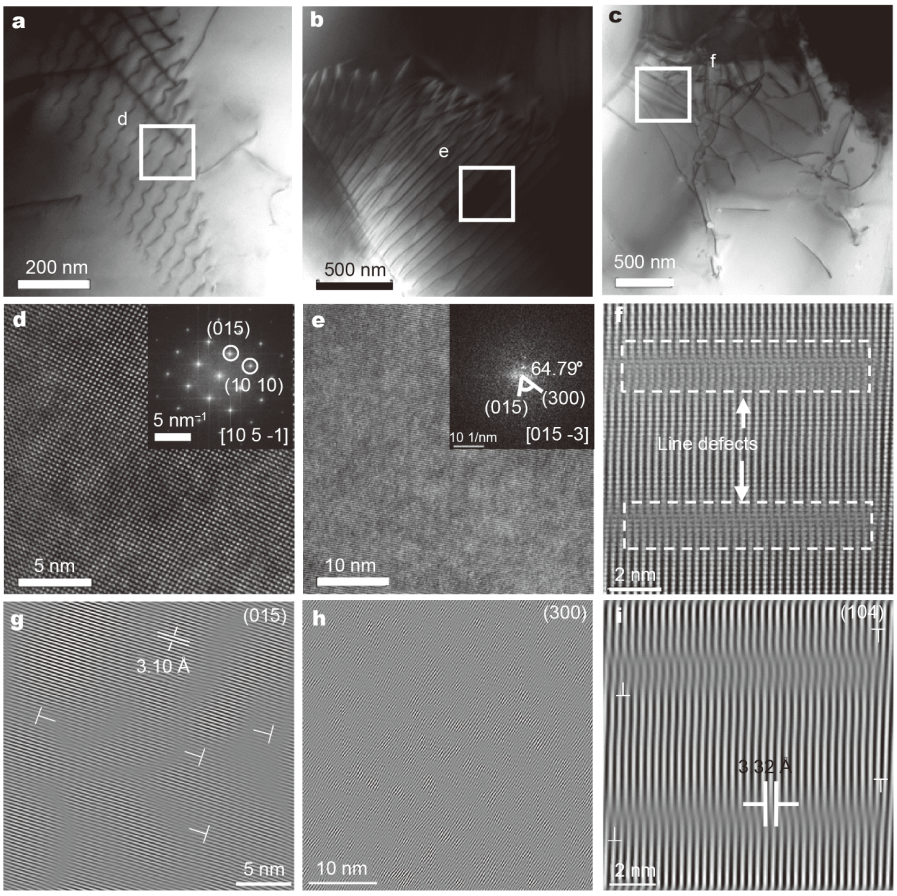

Figure 3 Different types of line defects in the $Bi_{0.4}Sb_{1.6}Te_{3.72}$ sample, observed on the plane perpendicular to the pressure direction. Low-magnified TEM images of three shapes of high-density line defects: (a) "S" type; (b) "X" type; (c) "Reticular" type, respectively. (d, e) HRTEM images of the enlarged regions of white boxes in Fig. 5a and b, respectively (insets denote their respective SAED images). (f) The atomically resolved STEM-HAADF image of the white box region in Fig. 5c. (g–i) IFFT images of (015), (300) and (104) atomic planes, corresponding to (d), (e) and (f), respectively, demonstrating the high-density line defects and lattice distortions.

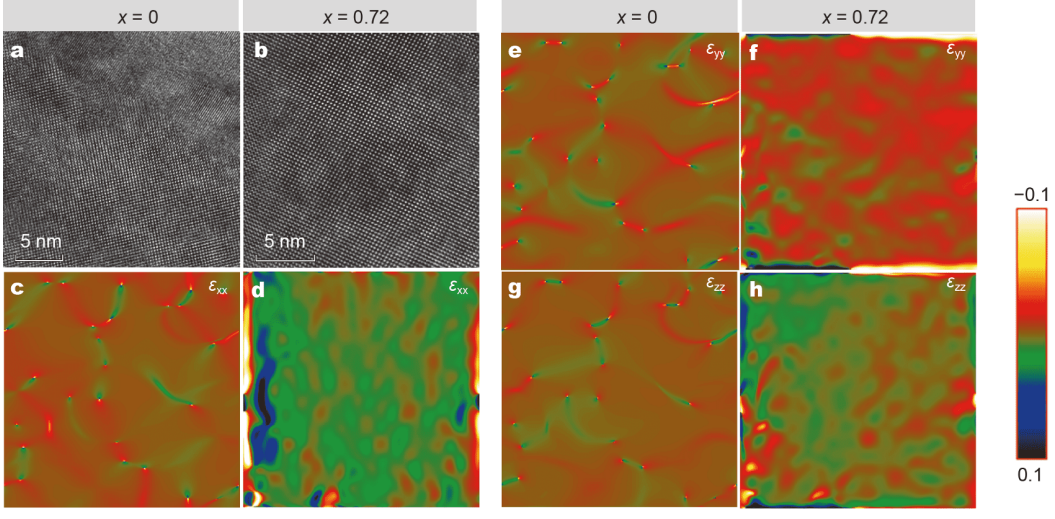

Figure 4 Comparison of the atomic strain distribution on planes perpendicular to the pressure direction between the $x = 0$ and $x = 0.72$ samples, based on their corresponding HRTEM images (a, b). The corresponding maps of (c, d) horizontal normal (ε_{xx}), (e, f) vertical normal (ε_{yy}) and (g, h) shear strains (ε_{xy}).

Following the meticulous observation of the TEM microstructure, it is still necessary to derive a comprehensive understanding of the following results, namely, (i) the texture enhancement with the rising Te excess, and (ii) the distribution and density of line defects exhibiting obvious anisotropies.

Firstly, the sintering pressure used in this research is only 40 MPa, significantly lower than the 70 MPa used in the report by Kim *et al.* [44]. During the densification process, the lower pressure gives rise to a larger gap between particles, leading to a better fluidity for the intergrain liquid phases. As compared with the pure solid-state sintering, the larger diffusion rate of atoms in the liquid phase makes the mass and heat transfer faster, promoting grain recrystallization [55]. Under the dual action of high temperature and axial sintering pressure, coupled with the capillary force in the flowing liquid on the grain surface, the greater plastic deformation of grains markedly promotes the grain rearrangement and simultaneously induces highly dense defects [56,57]. A part of the liquid phase recrystallizes into a bismuth telluride crystal, whilst the majority is extruded out. Thus, no excess Te remains inside the sintered bulk. It is reported that atoms will preferentially aggregate and crystallize along the (00*l*) atomic plane into a textured structure during the solidification process of Bi_2Te_3-based materials [39]. However, the premise is that there is an obvious external driving force, such as temperature gradient, axial pressure and strong magnetic field. In a certain range, the grain alignment is more pronounced when the content of the liquid phase is increased. However, an excessive amount of liquid will render it difficult for the sintering process to proceed and will result in a substantial loss of material [56]. The adjacent layers in the Bi_2Te_3 crystal are bonded by van der Waals forces, and the stacking fault energy of (00*l*) atomic plane is lower than that of other atomic planes [41]. The bonding of interlayer is thus prone to be imperfect during solidification or recrystallization, resulting in the generation of high-density line defects and lattice distortions on (00*l*)-oriented lattice planes. However, this concept does not apply to other oriented planes. The density and distribution of line defects, therefore, exhibit strong anisotropies.

Electrical transport properties

Fig. 5 presents the electronic transport properties of $Bi_{0.4}Sb_{1.6}Te_{3+x}$ bulk samples. Fig. 5a demonstrates that the electrical conductivity along the perpendicular plane ($\sigma_\perp$) is notably higher than $\sigma_{//}$. As the amount of Te rises, the $\sigma_\perp$ gradually increases; however, the trend is totally reversed in the parallel direction. The room temperature $\sigma_\perp$ of the x = 0.72 sample can reach up to 15×10^4 S m^{-1}, approximately 66.7% higher than $\sigma_{//}$, whereas for the x = 0 sample, the difference is only 6.21%. The increasing anisotropy in σ as the Te excess increases is primarily derived from the notable difference between carrier mobilities, as shown in Fig. 5d. When the texture is enhanced, the charge carrier transport along the pressure direction is substantially inhibited by scattering at grain boundaries and van der Waals interlayers. The mobility ($\perp$) of the x = 0.72 sample is up to 266 cm^2 V^{-1} s^{-1} at room temperature, approximately 35% higher than that of the x = 0 sample. Fig. 5b demonstrates that the Seebeck coefficient also exhibits a slight anisotropy. Meanwhile, the maximum Seebeck coefficients of all samples are obtained at approximately 400 K in both directions, indicating that the carrier concentrations of $Bi_{0.4}Sb_{1.6}Te_{3+x}$ samples are relatively close. Anisotropies in σ and S lead to a strong anisotropy in the PF, as shown in Fig. 5c. The maximum PF ($\perp$) values of all $Bi_{0.4}Sb_{1.6}Te_{3+x}$ samples are significantly larger than those along the parallel orientation and the anisotropy turns more obvious with the increasing excess of Te. The peak PF ($\perp$) for the $Bi_{0.4}Sb_{1.6}Te_3$ sample reaches up to 5 mW m^{-1} K^{-2} at room temperature, about 31% higher than that of the $Bi_{0.4}Sb_{1.6}Te_3$ sample. This value is also comparable to the highest value previously reported [58].

Fig. S10 presents the low-temperature electronic transport properties, measured within 10–300 K. The electrical conductivity in Fig. S10a displays a typical degenerated semiconductor transport behavior, namely the electrical conductivity decreases as temperature rises. The temperature dependence of the hole concentration is given in Fig. S10b, which shows that all samples have room-temperature hole concentrations between 3×10^{19} and 4×10^{19} cm^{-3}. As shown in Fig. S10c, carrier mobilities near room temperature can be approximately fitted to μ–$T^{-3/2}$, suggesting that the electron transport is primarily scattered by acoustic phonons. Fig. S10d demonstrates that the data points of carrier concentration and the Seebeck coefficient are all located on the Pisorenko plot ($m^* = 0.9m_0$). This result indicates that the band structures of all samples are almost identical. Thus, the differences of electronic transport properties between bulk samples are predominantly determined by the nature of the sample morphology.

Thermal transport properties and *ZT*

Fig. 6 presents the thermal transport properties of the $Bi_{0.4}Sb_{1.6}Te_{3+x}$ samples. With regard to Fig. 6a, it is evident

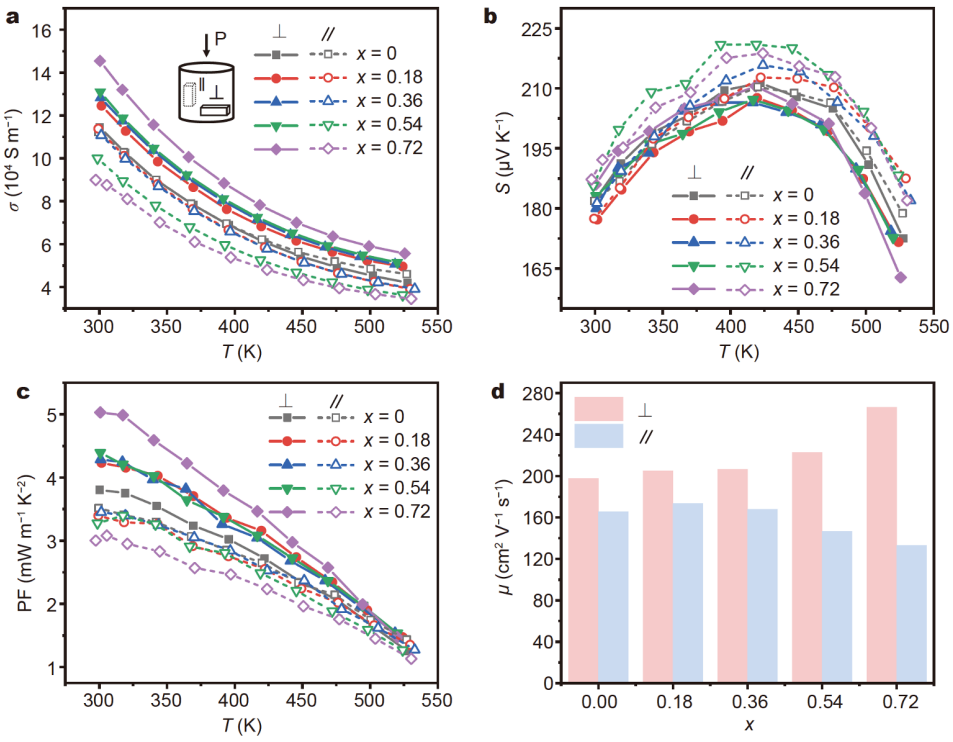

Figure 5 Temperature dependence of the (a) electrical, (b) Seebeck coefficient and (c) PF for the $Bi_{0.4}Sb_{1.6}Te_{3+x}$ bulk samples, measured perpendicular (solid lines with solid symbols, marked by ⊥) and parallel (dashed lines with open symbols, marked by //) to the pressure direction. (d) Relationship between the amount of excess Te and room-temperature mobilities of all samples.

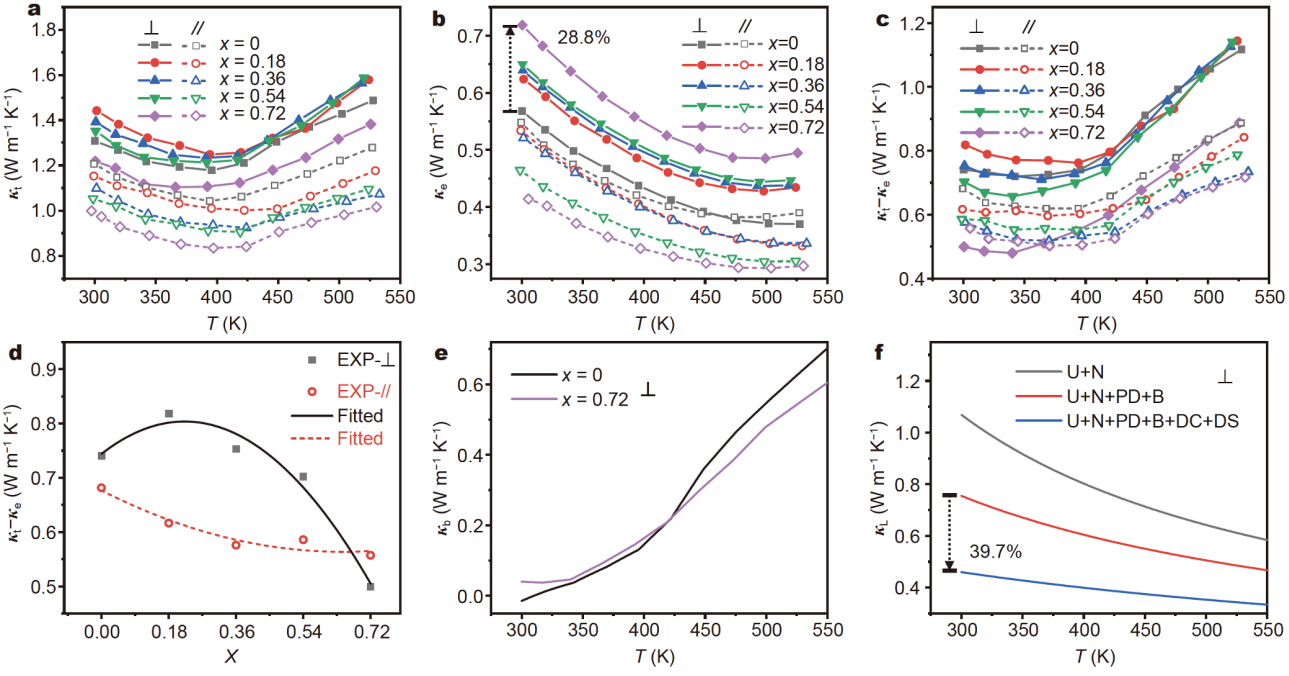

Figure 6 Temperature dependence of the (a) total thermal conductivity (κ_t), (b) electronic thermal conductivity (κ_e) and (c) nonelectronic thermal conductivity (κ_t–κ_e). (d) Relationship between the amount of excess Te and room-temperature κ_t–κ_e, the temperature dependence of the (e) bipolar thermal conductivity (κ_b) and (f) lattice thermal conductivity (κ_L) for the x = 0 and x = 0.72 samples.

that the total thermal conductivity exhibits a strong anisotropy as well. The relative density of all sintered samples exceeded 98.5%, as listed in Table S2. The experimentally determined heat capacity (C_p) of the $Bi_{0.4}Sb_{1.6}Te_{3.72}$ sample is shown in Fig. S11. The total thermal conductivity κ_t (⊥) initially increases and then decreases with the rising excess of Te. The electronic thermal conductivity κ_e is calculated by the Wiedemann-Franz law: $\kappa_e = L\sigma T$, where L is the Lorenz constant [16]. Under approximate conditions of the relaxation time and using a single parabolic band model, L can be determined by the following Equation (4):

$$L = \left(\frac{k_B}{e}\right)^2 \left[\frac{(r+7/2)F_{r+5/2}(\eta_F)}{(r+3/2)F_{r+1/2}(\eta_F)} - \delta^2(\eta_F)\right]. \quad (4)$$

The calculated results indicate that the values of L within 300–525 K are almost identical, approximately 1.5–1.6 W Ω K^{-2}. The calculated κ_e is provided in Fig. 6b. The κ_e (⊥) increases with the rising excess of Te; however, the trend is opposite for κ_e (//). It is worth noting that the total thermal conductivity κ_t includes contributions from the lattice part (κ_L), electronic part κ_e and the bipolar conductance (κ_b) [8]. In order to ascertain why the κ_t (⊥) decreases with the rise of Te excess when x is over 0.18, it is necessary to calculate the non-electronic thermal conductivity ($\kappa_L + \kappa_b$) using the formula $\kappa_L + \kappa_b = \kappa_t - \kappa_e$, as shown in Fig. 6c. It is worth acknowledging that due to the negligible bipolar thermal conductivity of p-BiSbTe alloys at approximately room temperature, the non-electronic thermal conductivity is equated with κ_L. Therefore, to obtain an in-depth understanding of the change of κ_L as the Te excess increases, the relationship between the amount of excess Te and room-temperature $\kappa_t - \kappa_e$ is given in Fig. 6d. It can be observed that κ_L begins to increase and then decreases with the increasing excess of Te, which is a result of the competing phonon scattering mechanisms. The initial rise of κ_L is due to the slightly weaker scattering of phonons from the enhanced texture. However, as the excess of Te rises, the density of line defects significantly increases. The size of the line defects is comparable to the wavelength of mid-frequency phonons [44]. Thus, a large number of phonons with intermediate frequencies would be scattered by the substantially increasing density of line defects [53]. Moreover, there is a distinct distortion in lattices near line defects, resulting in a strong fluctuation of the stress field, which strongly interferes with lattice vibrations. The κ_L (⊥) thus begins to decrease when x exceeds 0.18. As compared with the increase of ~28.8% in the room-temperature κ_e (⊥), the κ_L (⊥) demonstrates a sharper decrease of ~39.7%, leading to the overall reduction in κ_t (⊥). The κ_L (⊥) gradually decreases with the rising excess of Te due to stronger scattering by van der Waals layers caused by the enhanced texture.

It is observed that the κ_b (⊥) for the $x = 0$ and $x = 0.72$ samples are almost the same in the whole temperature range. To quantitatively evaluate the effect of line defects on reducing κ_L, the κ_L (⊥) of $x = 0$ and $x = 0.72$ samples were calculated by the Debye-Callaway model [59]. According to the model, the total inverse relaxation time τ_t^{-1} of phonons is the sum of the reciprocal relaxation time of each contributing scattering mechanism ($\tau_t^{-1} = \tau_U^{-1} + \tau_{PD}^{-1} + \tau_{GB}^{-1} + \tau_{DC}^{-1} + \tau_{DS}^{-1}$), including the Umklapp scattering process (τ_U), point defect scattering (τ_{PD}), grain boundary scattering (τ_{GB}), dislocation core scattering (τ_{DC}) and dislocation strain scattering (τ_{DS}). Detailed equations and related values of parameters for each scattering mechanism are listed in Equations S1–S13 and Table S3, respectively. Once the total relaxation time is determined, the κ_L can be obtained according to Equation (5) [60]:

$$\kappa_L = \frac{k_B}{2\pi^2 v}\left(\frac{k_B T}{\hbar}\right)^3 \int_0^{\theta_D/T} \tau_t(x)\frac{x^4 e^x}{(e^x-1)^2}dx, \quad (5)$$

where x, ω, v and θ_D are the reduced Fermi level ($x = \hbar\omega/k_B T$), phonon frequency, average phonon velocity and Debye temperature, respectively. The κ_b for $x = 0$ and $x = 0.72$ samples were determined by subtracting the electronic and lattice thermal conductivities from κ_t, as shown in Fig. 6e. The result demonstrates that the κ_b (⊥) in two samples are essentially the same throughout the whole temperature range. The calculated κ_L (⊥), including different participating scattering mechanisms, is shown in Fig. 6f. As can be observed, aside from the point defects and grain boundaries, the highly dense dislocations can also reduce κ_L very effectively. Therefore, compared with the $x = 0$ sample, it is the high-density line defects that abruptly reduces the κ_t of the $x = 0.72$ sample.

According to the electronic and thermal transport properties, the quality factor defined as $\mu/(k_t - k_e)$ can be used to evalutate the approximate room-temperature TE properties [8]. Meanwhile, the ZT and average ZT in the temperature range from 300 to 525 K were calculated. The average ZT can be obtained from Equation (6):

$$ZT_{avg} = \int_{T_1}^{T_2} ZT\,dT/(T_2 - T_1), \quad (6)$$

where T_1 and T_2 are the lowest and the highest measuring temperatures, respectively. As shown in Fig. 7a, the quality factor (⊥) gradually increases and surpasses that

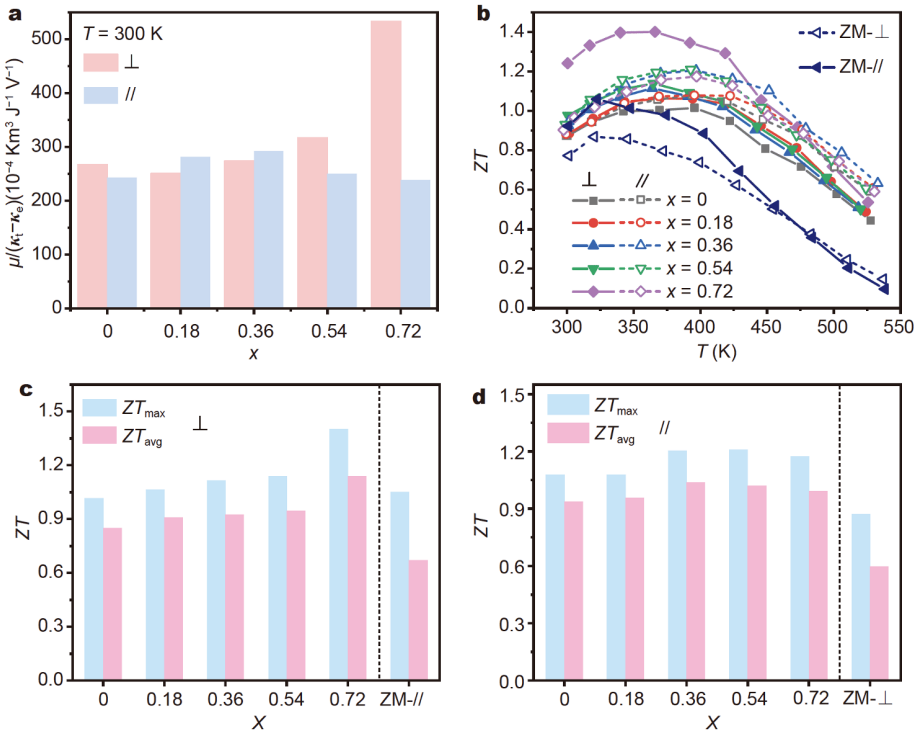

Figure 7 (a) Relationship between room-temperature quality factor and the amount of excess Te. (b) Temperature dependence of the *ZT* values of SPS-sintered $Bi_{0.4}Sb_{1.6}Te_{3+x}$ samples and commercially ZM-prepared $Bi_{0.5}Sb_{1.5}Te_3$ ingot. The maximum *ZT* and average *ZT* values of the $Bi_{0.4}Sb_{1.6}Te_{3+x}$ bulk samples obtained by TER-SPS technique and ZM-prepared $Bi_{0.5}Sb_{1.5}Te_3$ single crystals are compared as well. ZM-// and ZM-⊥ denote the ZM-prepared samples parallel (//) and perpendicular (⊥) to the direction along applied temperature gradient, respectively.

of the parallel direciton (//) as the excess Te increases. Benefiting from the simultaneous optimization of the electrical and thermal conductivities, the maximum *ZT* for the $x = 0.72$ sample can reach up to 1.4 at 350 K, approximately 22% and 40% higher than that of the $x = 0$ sample and the commercial ZM ingot, respectively, as shown in Fig. 7b. Fig. 7c, d display the ZT_{max} and ZT_{avg} values of all samples in perpendicular (⊥) and parallel (//) directions, respectively. Both the ZT_{max} (⊥) and ZT_{avg} (⊥) increase notably with the increasing excess of Te. However, in the parallel direction, they slowly increase initially but then gradually decrease with the increasing Te excess. Furthermore, the homogeneity of the room-temperature Seebeck coefficient and the reproducibility of the TE properties as a function of temperature for the $Bi_{0.4}Sb_{1.6}Te_{3.72}$ sample are documented in Figs S12 and S13, respectively.

Mechanical properties

The processability, utilization rate, service life and material cost all depend to a considerable extent on the mechanical properties of the structure. This is particularly apparent for intrinsically brittle TE materials, as they are subjected to multiple processing procedures. Therefore, poor mechanical performance will significantly hinder their large-scale applications [28,33]. As such, the mechanical properties of $x = 0$ and $x = 0.72$ samples in the present study were measured and compared. The measured compressive strength is given in Fig. 8. The compressive stress-strain curves, as displayed in Fig. 8a, demonstrate the brittle fracture features of both samples. It is noted that the maximum compressive strength for the $x = 0.72$ sample can reach up to 100 MPa. Furthermore, the average compressive strengths of the $Bi_{0.4}Sb_{1.6}Te_{3.72}$ sample and other p-BiSbTe materials prepared by several techniques are compared in Fig. 8b. Similar to the Bi_2Te_3-based materials prepared by the zone-melting and selective laser melting (SLM) methods, the $Bi_{0.4}Sb_{1.6}Te_{3.72}$ sample also exhibits obvious anisotropy for compressive strength, which originates from its texture characteristic. On the contrary, the p-BiSbTe samples prepared by the thermally induced flash synthesis combined with SPS (TIFS-SPS) [30] and MS-SPS [33] techniques exhibit isotropies due to their loss of texture in

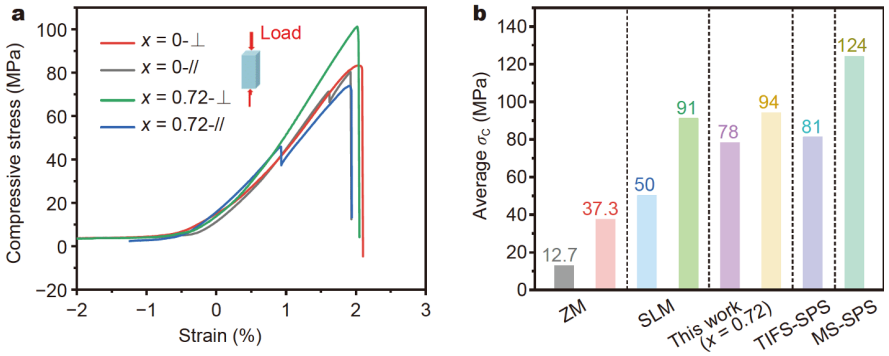

Figure 8 (a) The representative compressive stress-strain curves of the $Bi_{0.4}Sb_{1.6}Te_3$ and $Bi_{0.4}Sb_{1.6}Te_{3.72}$ samples measured parallel and perpendicular to the pressure direction. (b) The comparison of average compressive strengths for the p-BiSbTe samples prepared by several typical methods. The parameter *F* listed in the top of (b) denotes the orientation factor of their respective bulk samples.

microstructure. The average compressive strength of more than 10 $Bi_{0.4}Sb_{1.6}Te_{3.72}$ samples along the perpendicular direction is 94 MPa, significantly higher than that of the ZM ingots. From Fig. 8b, it is concluded that for the p-BiSbTe sample, the higher the degree of the texture, the greater the compressive strength anisotropy. In comparison with the $Bi_{0.4}Sb_{1.6}Te_3$ sample, the much-improved mechanical strength of the $Bi_{0.4}Sb_{1.6}Te_{3.72}$ sample is potentially a result of the high density of the dislocations. The dislocation theory affirms that the overall slip of the lattice is realized just by the movement of dislocation lines. As a consequence, dense dislocations inside grains will make it easier for the lattice to deform when an external force is applied. Numerous dislocations would also make their own movements more complex and difficult, such as dislocation pile-ups, jogs and twists, which can enhance the deformation resistances and yield strengths of bulk materials. The result in this work proves that the compressive strength of the $Bi_{0.4}Sb_{1.6}Te_3$ compound can be effectively optimized by introducing an additional 24 mol% Te.

To verify that the $Bi_{0.4}Sb_{1.6}Te_{3.72}$ sample is appropriate for use in the fabrication of micro-TE devices, it is necessary to focus on its machinability during the precise cutting process with a diamond blade. Under the same parameters, namely the blade rotation speed and cutting velocity, different sizes of TE legs were obtained by cutting $Bi_{0.4}Sb_{1.6}Te_{3.72}$ and ZM-prepared bulk samples with varying cut spacing. Their mechanical properties were qualitatively compared by observing the integrity of the cutting TE legs. The cutting depth direction was controlled parallel to the grain-preferred direction of their respective bulk samples. In Fig. S14a, all legs of the ZM sample are broken when the leg width is less than 0.6 mm, which is ascribed to the large shear stress parallel to the cleavage plane greatly exceeding the maximum shear strength. By contrast, most legs cut from the $Bi_{0.4}Sb_{1.6}Te_{3.72}$ sample, shown in Fig. S14b, remain intact and the minimum width of the legs could be as low as 0.1 mm. Fig. S14c, d present the facture plane morphologies of ZM and $Bi_{0.4}Sb_{1.6}Te_{3.72}$ legs, respectively. In Fig. S14c, the ZM ingot presents a relatively large lamellar grain in parallel to each other. However, as illustrated in Fig. S14d, the $Bi_{0.4}Sb_{1.6}Te_{3.72}$ sample exhibits much smaller sized grains aligned on the plane perpendicular to the pressure direction. In summary, the $Bi_{0.4}Sb_{1.6}Te_{3.72}$ sample demonstrates much superior machinability during cutting, implying that it has a considerable potential as a substance employed for the fabrication of miniature TE modules.

CONCLUSIONS

In the present study, we prepared a series of $Bi_{0.4}Sb_{1.6}Te_{3+x}$ bulk alloys using the TER-SPS technique for the first time. It is found that the Te excess in the as-synthesized product is distributed randomly in the form of the eutectic phase and free Te. The flowing liquid phase tends to wet grains during plastic deformation and facilitate grain rearrangement as well as recrystallization. The resulting increased texture significantly enhances the carrier mobility. Meanwhile, the liquid phase significantly increases the density of line defects on the perpendicular plane. Finally, the orientation factor, ZT_{max} and compressive mechanical strength of the $Bi_{0.4}Sb_{1.6}Te_{3.72}$ sample are 0.25, 1.4 and 94 MPa, respectively, representing 25%, 22%, and 16% higher values than the $Bi_{0.4}Sb_{1.6}Te_3$ sample. The minimum leg width obtained by cutting the $Bi_{0.4}Sb_{1.6}Te_{3.72}$ specimen can be as small as 0.1 mm, far exceeding that achievable by cutting the ZM ingot. This result proves that the $Bi_{0.4}Sb_{1.6}Te_{3.72}$ sample is eminently suitable for the

fabrication of miniature TE modules. This work demonstrates that the simultaneous optimization of the texture, TE and mechanical properties of p-BiSbTe materials can be realized through a simple and effective TER-SPS technique.

Received 1 September 2020; accepted 26 October 2020; published online 18 January 2021

1 Snyder GJ, Toberer ES. Complex thermoelectric materials. Nat Mater, 2008, 7: 105–114
2 Pei Y, Shi X, LaLonde A, *et al.* Convergence of electronic bands for high performance bulk thermoelectrics. Nature, 2011, 473: 66–69
3 Biswas K, He J, Blum ID, *et al.* High-performance bulk thermoelectrics with all-scale hierarchical architectures. Nature, 2012, 489: 414–418
4 Zhao LD, Tan G, Hao S, *et al.* Ultrahigh power factor and thermoelectric performance in hole-doped single-crystal SnSe. Science, 2016, 351: 141–144
5 Andrews JG, Buzzi S, Choi W, *et al.* What will 5G be? IEEE J Sel Areas Commun, 2014, 32: 1065–1082
6 Yu E, Wang D, Kim S, *et al.* Active cooling of integrated circuits and optoelectronic devices using a micro configured thermoelectric and fluidic system. In: Proceedings of Inter Society Conference on Thermal Phenomena. New Orleans, Louisiana, USA, 2000, 134–139
7 Lv H, Yu Y, Huang D, *et al.* A fast optical wavelength-tunable transmitter with a linear thermoelectric cooler driver. IEEE Electron Device Lett, 2009, 30: 353–355
8 He J, Tritt TM. Advances in thermoelectric materials research: Looking back and moving forward. Science, 2017, 357: eaak9997
9 Shi X, Chen H, Hao F, *et al.* Room-temperature ductile inorganic semiconductor. Nat Mater, 2018, 17: 421–426
10 Mao J, Zhu H, Ding Z, *et al.* High thermoelectric cooling performance of n-type Mg_3Bi_2-based materials. Science, 2019, 365: 495–498
11 He W, Wang D, Wu H, *et al.* High thermoelectric performance in low-cost $SnS_{0.91}Se_{0.09}$ crystals. Science, 2019, 365: 1418–1424
12 Xie H, Su X, Yan Y, *et al.* Thermoelectric performance of $CuFeS_{2+2x}$ composites prepared by rapid thermal explosion. NPG Asia Mater, 2017, 9: e390
13 Xiao Y, Zhao LD. Seeking new, highly effective thermoelectrics. Science, 2020, 367: 1196–1197
14 Poudel B, Hao Q, Ma Y, *et al.* High-thermoelectric performance of nanostructured bismuth antimony telluride bulk alloys. Science, 2008, 320: 634–638
15 Xie H, Su X, Zhang X, *et al.* Origin of intrinsically low thermal conductivity in talnakhite $Cu_{17.6}Fe_{17.6}S_{32}$ thermoelectric material: Correlations between lattice dynamics and thermal transport. J Am Chem Soc, 2019, 141: 10905–10914
16 Xie H, Su X, Zheng G, *et al.* The role of Zn in chalcopyrite $CuFeS_2$: Enhanced thermoelectric properties of $Cu_{1-x}Zn_xFeS_2$ with *in situ* nanoprecipitates. Adv Energy Mater, 2017, 7: 1601299
17 Tan G, Zhao LD, Kanatzidis MG. Rationally designing high-performance bulk thermoelectric materials. Chem Rev, 2016, 116: 12123–12149
18 Heremans JP, Jovovic V, Toberer ES, *et al.* Enhancement of thermoelectric efficiency in PbTe by distortion of the electronic density of states. Science, 2008, 321: 554–557
19 Chandra S, Biswas K. Realization of high thermoelectric figure of merit in solution synthesized 2D SnSe nanoplates *via* Ge alloying. J Am Chem Soc, 2019, 141: 6141–6145
20 Samanta M, Ghosh T, Chandra S, *et al.* Layered materials with 2D connectivity for thermoelectric energy conversion. J Mater Chem A, 2020, 8: 12226–12261
21 Sarkar D, Ghosh T, Roychowdhury S, *et al.* Ferroelectric instability induced ultralow thermal conductivity and high thermoelectric performance in rhombohedral p-type GeSe crystal. J Am Chem Soc, 2020, 142: 12237–12244
22 Fang T, Li X, Hu C, *et al.* Complex band structures and lattice dynamics of Bi_2Te_3-based compounds and solid solutions. Adv Funct Mater, 2019, 29: 1900677
23 Ben-Yehuda O, Shuker R, Gelbstein Y, *et al.* Highly textured Bi_2Te_3-based materials for thermoelectric energy conversion. J Appl Phys, 2007, 101: 113707
24 Zebarjadi M, Esfarjani K, Dresselhaus MS, *et al.* Perspectives on thermoelectrics: From fundamentals to device applications. Energy Environ Sci, 2012, 5: 5147–5162
25 Goldsmid HJ. Introduction to Thermoelectricity. Sydney: Springer, 2009
26 Rowe DM (eds). CRC Handbook of Thermoelectrics. Florida: CRC Press, 1995
27 Shen JJ, Zhu TJ, Zhao XB, *et al.* Recrystallization induced *in situ* nanostructures in bulk bismuth antimony tellurides: A simple top down route and improved thermoelectric properties. Energ Environ Sci, 2010, 3: 1519–1523
28 Zheng Y, Xie H, Shu S, *et al.* High-temperature mechanical and thermoelectric properties of p-type $Bi_{0.5}Sb_{1.5}Te_3$ commercial zone melting ingots. J Elec Materi, 2013, 43: 2017–2022
29 Zhu T, Xu Z, He J, *et al.* Hot deformation induced bulk nanostructuring of unidirectionally grown p-type $(Bi,Sb)_2Te_3$ thermoelectric materials. J Mater Chem A, 2013, 1: 11589–11594
30 Zheng G, Su X, Xie H, *et al.* High thermoelectric performance of p-BiSbTe compounds prepared by ultra-fast thermally induced reaction. Energy Environ Sci, 2017, 10: 2638–2652
31 Xie W, Tang X, Yan Y, *et al.* Unique nanostructures and enhanced thermoelectric performance of melt-spun BiSbTe alloys. Appl Phys Lett, 2009, 94: 102111
32 Deng R, Su X, Hao S, *et al.* High thermoelectric performance in $Bi_{0.46}Sb_{1.54}Te_3$ nanostructured with ZnTe. Energy Environ Sci, 2018, 11: 1520–1535
33 Zheng Y, Zhang Q, Su X, *et al.* Mechanically robust BiSbTe alloys with superior thermoelectric performance: A case study of stable hierarchical nanostructured thermoelectric materials. Adv Energy Mater, 2015, 5: 1401391
34 Tao Q, Deng R, Li J, *et al.* Enhanced thermoelectric performance of $Bi_{0.46}Sb_{1.54}Te_3$ nanostructured with CdTe. ACS Appl Mater Interfaces, 2020, 12: 26330–26341
35 Bao D, Chen J, Yu Y, *et al.* Texture-dependent thermoelectric properties of nano-structured Bi_2Te_3. Chem Eng J, 2020, 388: 124295
36 Wang M, Tang Z, Zhu T, *et al.* The effect of texture degree on the anisotropic thermoelectric properties of $(Bi,Sb)_2(Te,Se)_3$ based solid solutions. RSC Adv, 2016, 6: 98646–98651
37 Mu X, Zhou H, He D, *et al.* Enhanced electrical properties of stoichiometric $Bi_{0.5}Sb_{1.5}Te_3$ film with high-crystallinity *via* layer-by-layer *in-situ* growth. Nano Energy, 2017, 33: 55–64
38 Concepción O, Tavira A, Roque J, *et al.* Texture analysis and epitaxial relationships in Bi_2Te_3 thin film grown by physical vapor

transport on silicon substrates. Appl Surf Sci, 2019, 464: 280–286
39 Qiu J, Yan Y, Luo T, *et al.* 3D printing of highly textured bulk thermoelectric materials: Mechanically robust BiSbTe alloys with superior performance. Energy Environ Sci, 2019, 12: 3106–3117
40 Mao Y, Yan Y, Wu K, *et al.* Non-equilibrium synthesis and characterization of n-type $Bi_2Te_{2.7}Se_{0.3}$ thermoelectric material prepared by rapid laser melting and solidification. RSC Adv, 2017, 7: 21439–21445
41 Luo Y, Yang J, Jiang Q, *et al.* Melting and solidification of bismuth antimony telluride under a high magnetic field: A new route to high thermoelectric performance. Nano Energy, 2015, 15: 709–718
42 Jiang J, Chen L, Bai S, *et al.* Fabrication and thermoelectric performance of textured n-type $Bi_2(Te,Se)_3$ by spark plasma sintering. Mater Sci Eng-B, 2005, 117: 334–338
43 Shen JJ, Hu LP, Zhu TJ, *et al.* The texture related anisotropy of thermoelectric properties in bismuth telluride based polycrystalline alloys. Appl Phys Lett, 2011, 99: 124102
44 Kim SI, Lee KH, Mun HA, *et al.* Dense dislocation arrays embedded in grain boundaries for high-performance bulk thermoelectrics. Science, 2015, 348: 109–114
45 Pan Y, Aydemir U, Grovogui JA, *et al.* Melt-centrifuged $(Bi,Sb)_2Te_3$: Engineering microstructure toward high thermoelectric efficiency. Adv Mater, 2018, 30: 1802016
46 Hwang JY, Kim J, Kim HS, *et al.* Effect of dislocation arrays at grain boundaries on electronic transport properties of bismuth antimony telluride: Unified strategy for high thermoelectric performance. Adv Energy Mater, 2018, 8: 1800065
47 Zhang C, de la Mata M, Li Z, *et al.* Enhanced thermoelectric performance of solution-derived bismuth telluride based nanocomposites *via* liquid-phase sintering. Nano Energy, 2016, 30: 630–638
48 Pan Y, Qiu Y, Witting I, *et al.* Synergistic modulation of mobility and thermal conductivity in $(Bi,Sb)_2Te_3$ towards high thermoelectric performance. Energy Environ Sci, 2019, 12: 624–630
49 Xu ZJ, Hu LP, Ying PJ, *et al.* Enhanced thermoelectric and mechanical properties of zone melted p-type $(Bi,Sb)_2Te_3$ thermoelectric materials by hot deformation. Acta Mater, 2015, 84: 385–392
50 Zhai R, Hu L, Wu H, *et al.* Enhancing thermoelectric performance of n-type hot deformed bismuth-telluride-based solid solutions by nonstoichiometry-mediated intrinsic point defects. ACS Appl Mater Interfaces, 2017, 9: 28577–28585
51 Wu Y, Yu Y, Zhang Q, *et al.* Liquid-phase hot deformation to enhance thermoelectric performance of n-type bismuth-telluride-based solid solutions. Adv Sci, 2019, 6: 1901702
52 Mion C, Muth JF, Preble EA, *et al.* Thermal conductivity, dislocation density and GaN device design. Superlattices MicroStruct, 2006, 40: 338–342
53 Klemens PG. The scattering of low-frequency lattice waves by static imperfections. Proc Phys Soc A, 1955, 68: 1113–1128
54 Deng R, Su X, Zheng Z, *et al.* Thermal conductivity in $Bi_{0.5}Sb_{1.5}Te_{3+x}$ and the role of dense dislocation arrays at grain boundaries. Sci Adv, 2018, 4: eaar5606
55 Peterson NL. Grain-boundary diffusion in metals. Int Met Rev, 1983, 28: 65–91
56 German RM, Suri P, Park SJ. Review: Liquid phase sintering. J Mater Sci, 2009, 44: 1–39
57 Gao Z, Xiong Z, Li J, *et al.* Enhanced thermoelectric performance of higher manganese silicides by shock-induced high-density dislocations. J Mater Chem A, 2019, 7: 3384–3390
58 Kim YM, Lydia R, Kim JH, *et al.* Enhancement of thermoelectric properties in liquid-phase sintered Te-excess bismuth antimony tellurides prepared by hot-press sintering. Acta Mater, 2017, 135: 297–303
59 Callaway J, von Baeyer HC. Effect of point imperfections on lattice thermal conductivity. Phys Rev, 1960, 120: 1149–1154
60 Callaway J. Model for lattice thermal conductivity at low temperatures. Phys Rev, 1959, 113: 1046–1051

Acknowledgements This work was financially supported by the National Key Research and Development Program of China (2018YFB0703600), the National Natural Science Foundation of China (51772232), the 111 Project of China (B07040), and Wuhan Frontier Project on Applied Research Foundation (2019010701011405).

Author contributions Qiu J, Yan Y, Xie H, Zhang M and Zhu T prepared the samples, designed and carried out the measurements of TE properties. Luo T, Xia F and Wu J conducted the HRTEM observation and analysis. Qiu J, Yan Y, Su X, Jiang H, Uher C, Xie H, and Tang X analyzed the electrical and thermal transport data, wrote and revised the manuscript. All authors have received, discussed and approved the results and conclusions of this article.

Conflict of interest The authors declare that they have no conflict of interest.

Supplementary information Experimental details and supporting data are available in the online version of the paper.

Junhao Qiu received his BS degree from Wuhan University of Science and Technology (WHUT) in 2015. He is currently a PhD candidate at the State Key Laboratory of Advanced Technology for Materials Synthesis and Processing, WHUT, China. His research interests focus on Bi_2Te_3 thermoelectric materials and additive manufacturing.

Yonggao Yan is a Professor at Wuhan University of Technology. He received his PhD in 2007 from WHUT, China. He joined WHUT after graduation. Then he worked at the National Institute of Standards and Technology (NIST) in USA as a guest researcher from 2009 to 2012, focusing on thermoelectric combinatorial metrology. His research topics cover the preparation and characterization of new thermoelectric materials *via* novel techniques like 3D printing, melting spinning, and rapid non-equilibrium synthesis.

Xinfeng Tang received his PhD from Tohoku University in 2000. He joined WHUT as a full professor in April 2001 and became a Chair Professor of materials science in 2011. Now he is working at the State Key Laboratory of Advanced Technology for Materials Synthesis and Processing and Director for the Advanced Materials Research Institute. He has been awarded as a Fellow of the American Physical Society as well as the Royal Society of Chemistry for his outstanding contributions in the fields of thermoelectric materials and devices.

通过增强织构和诱导高密度线缺陷获得优异性能的$Bi_{0.4}Sb_{1.6}Te_{3.72}$热电材料

邱俊豪[1], 鄢永高[1*], 谢鸿耀[2], 罗婷婷[1], 夏凡杰[1], 姚磊[1], 张敏[1], 祝婷[1], 谭刚健[1], 苏贤礼[1], 吴劲松[3], Ctirad Uher[4], 姜洪义[1], 唐新峰[1*]

摘要 商业化的区熔(ZM)Bi_2Te_3基单晶锭体力学性能差、热电转换效率不足, 一直阻碍着高效热电器件的微型化. 本文将超快速热爆反应与放电等离子体烧结技术相结合, 成功制备出了高强度、高热电性能的$Bi_{0.4}Sb_{1.6}Te_{3.72}$块体合金. 我们观察到, 引入过量Te不仅增强了(00*l*) 织构, 使得材料室温功率因子高达5 mW m^{-1} K^{-2}, 而且还诱导了密度高达10^{11}–10^{12} cm^{-2}的线缺陷. 与电子热导率的增加幅度相比, 如此高浓度的线缺陷使得晶格热导率下降的幅度更大, 致使总热导明显降低. 最终, $Bi_{0.4}Sb_{1.6}Te_{3.72}$材料在350 K下最大*ZT*值可达1.4, 比商业ZM锭体高出40%. 此外, 这种高密度的线缺陷还提升了材料的机械抗压强度, 其最大抗压强度为94 MPa, 比ZM单晶高出154%. 本文为Bi_2Te_3基热电材料的织构、热电性能及力学性能的协同优化提供了一种简单有效的策略, 也为微型化热电器件的商业化开发奠定了重要基础.